Generalizing bicubic splines for modelling and IGA with irregular layout

Kęstutis Karčiauskas[a] and Thien Nguyen[b] and Jörg Peters[b]

[a] Vilnius University   [b] University of Florida

Abstract

Quad meshes can be interpreted as tensor-product spline control meshes as long as they form a regular grid, locally. We present a new option for complementing bi-3 splines by bi-4 splines near irregularities in the mesh layout, where less or more than four quadrilaterals join. These new generalized surface and IGA (isogeometric analysis) elements have as their degrees of freedom the vertices of the irregular quad mesh. From a geometric design point of view, the new construction distinguishes itself from earlier work by a notably better distribution of highlight lines. From the IGA point of view, increased smoothness and reproduction at the irregular point yield fast convergence.

1. Introduction

A key task in extending tensor-product splines to more general control nets is building n-sided multi-spline caps that smoothly glue together n individual tensor-product splines. Such spline caps are central both for building geometrically smooth (G^k) free-form surfaces with irregular points, where less or more than four tensor-product patches join together – and to define the physical domain and the analysis functions for iso-parametric [IZ68] or isogeometric analysis (IGA) [HCB05] in the presence of irregular points.

The contribution of this paper is a new

- polynomial piecewise tensor-product cap construction of degree bi-4 that G^1 smoothly joins together bi-3 (bi-cubic) splines,

- results in a good highlight line distribution, better for $n = 3$ and some higher n than the curvature continuous bi-7 caps of [LS08] and

- yields high-order convergent IGA elements, one per vertex of the input quad mesh, for solving higher-order partial differential equations, such as thin shell problems.

Overview. After the literature review, Section 2 defines the setup and tools: multi-sided surface caps, geometric continuity and shape functionals. Section 3 presents the main construction yielding a G^1 surface of degree bi-4 for n-sided caps where $n = 5, 6, 7$. As always, special care has to be taken for the case $n = 3$ (Section 4) where the results improve even on constructions of much higher degree. Section 5 addresses caps of valence $n \geq 7$. Section 6 tests the isogeometric elements derived from the new construction.

1.1. Related work

The literature offers a number of algorithms for complementing tensor-product splines. These range from Catmull-Clark surfaces [CC78] to the sophisticated patch-based curvature continuous construction of degree bi-7 [LS08]. We compare our new construction to these canonical ones on a collection of challenging test data.

Older as well as most newer constructions of *low* polynomial degree, e.g. [GZ94, WN01, SSE$^+$13, BH14, BM], differ from the proposed construction in that they parametrically C^1 extend the tensor-product patches into the cap. Recent progress in surface constructions [KP14, KP15a] has shown that, for low degree and few patches, immediate reparameterization of the boundary data is necessary to obtain good shape. We also include in the comparison [LSNC09], an adaptation of Gregory's construction [Gre74] that is formally rational of degree bi-3.

The new bi-4 construction also differs from the bi-4 constructions in [WN01, SSE$^+$13, BM] in that it does not require solving equations for each new input to obtain the surface: evaluation and differentiation are explicit in terms of the vertices of the input quadrilateral (control-)net, a fact that comes in handy when constructing stiffness matrices for solving higher-order partial differential equations on manifolds. We compare the isogeometric elements based on the new construction in particular with the results in [NKP14].

The construction [KP14] mentioned earlier shows that multisided holes in a bi-2 (bi-quadratic) spline complex can be smoothly filled using caps of n spline patches that are of degree at most bi-4. However, the bi-2 degree of the underlying spline is crucial for the construction and [KP14] cannot be applied to complete the more widely-used bi-cubic tensor-product spline complexes.

2. Definitions and Setup

As a standard abstraction from the real-life complexity of blending trimmed surfaces, we consider a network of quadrilateral facets or *quads* that outline the final surface. Such a quad mesh might, for example, arise from Catmull-Clark subdivision. Interior mesh nodes where more or fewer than the regular

number of four quads meet are called *irregular nodes*. They are 1-1 related to *irregular points* where three or more than four surface patches meet. We assume that each irregular node is surrounded by at least one layer of regular i.e. 4-valent nodes and apply one step of Catmull-Clark subdivision should this not be the case. A *CC-net* $\mathbf{c}$ is a submesh consisting of the irregular node and $6n$ nodes that form two layers of quads surrounding it. (The second layer is allowed to have irregular nodes.) Fig. 1a displays a CC-net and Fig. 1c displays an *extended CC-net*, i.e. CC-net plus one additional layer of quads. This additional layer is not used for the construction of the cap but provides a surface ring (green in Fig. 1d) surrounding the cap. This ring allows judging the transition from the spline complex into the cap, a transition that is as important as the internal quality of the cap itself. The nodes of a CC-net will act like the control points of a tensor-product spline.
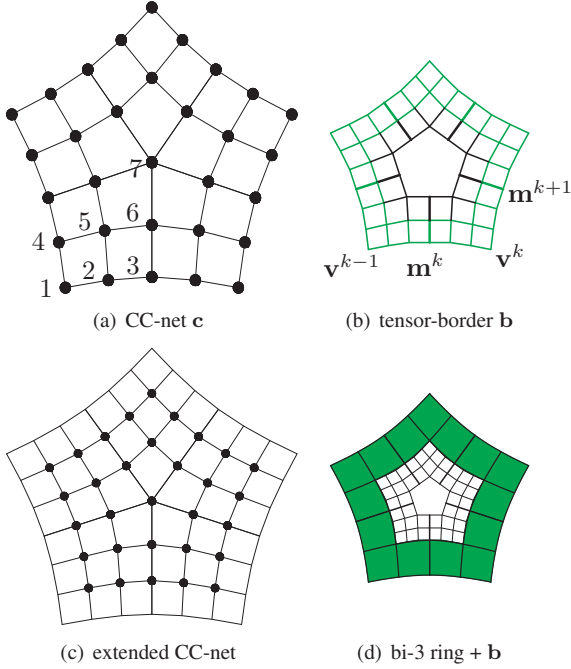

(a) CC-net $\mathbf{c}$ (b) tensor-border $\mathbf{b}$

(c) extended CC-net (d) bi-3 ring + $\mathbf{b}$

Figure 1: **Input.** (a) A CC-net $\mathbf{c}$ for $n = 5$ or, alternatively, (b) its corresponding **tensor-border** $\mathbf{b}$ of depth 2 represented in terms of BB-coefficients of degree bi-3. (c) Extended CC-net and (d) regular bi-3 surface layer (green) surrounding the tensor-border. In (a) the CC-net points of one sector are enumerated. In (b) the labels reference the corner vertices and the midpoints of the tensor-border.

2.1. Surface representation

A tensor-product patch $\mathbf{f}$ of bi-degree d is defined by its Bernstein-Bézier (BB) coefficients $\mathbf{f}_{ij}$ as

$$\mathbf{f}(u,v) := \sum_{i=0}^{d} \sum_{j=0}^{d} \mathbf{f}_{ij} B_i^d(u) B_j^d(v), \quad (u,v) \in \square := [0..1]^2,$$

where $B_k^d(t)$ is the kth Bernstein-Bézier polynomial of degree d. Since each 4×4 sub-grid of points of the network is interpreted as the B-spline control net of one bicubic

piece of a tensor-product spline surface, the well-known formulas of a B-spline to Bernstein-Bézier (BB)-form conversion [Far02, PBP02] can be applied to the CC-net, except at the irregular node. This provides Hermite data in bi-degree 3 form (see Fig. 1b,d) along the boundary of the cap. We refer to these Hermite data in the following as the *tensor-border* $\mathbf{b}$ (of depth 2 and degree 3). While our cap will only match the first derivatives defined by $\mathbf{b}$ (after a change of variables), its second-order Hermite data will enter via samples of a bi-5 guide surface that propagates curvature from the boundary into the cap.

To explain the algorithmic steps, it will be convenient to capture position and derivatives at a corner point $\mathbf{s}$ of a surface patch $\mathbf{f}$,

$$\mathbf{j}_{\mathbf{s},k}\mathbf{f} := \left[\partial_u^i \partial_v^j \mathbf{f}(\mathbf{s})\right]_{i,j \in \{0,1,\ldots,k\}}, \quad \partial_t^l \mathbf{f} := \frac{d^l \mathbf{f}}{(dt)^l}$$

in terms of its BB-coefficients $\mathbf{f}_{ij}$. For $k \leq d+1$ and $\mathbf{s} := \mathbf{f}(0,0)$, the $k \times k$ BB-sub-net

$$\mathbf{J}_{\mathbf{s},k}^d \mathbf{f} := \left[\mathbf{f}_{ij}\right]_{i,j \in \{0,1,\ldots,k\}}$$

contains complete information about $\mathbf{j}_{\mathbf{s},k}\mathbf{f}$ at $\mathbf{s}$, expressed in BB-form of degree bi-d. For example, $\mathbf{f}_{00}$, $\mathbf{f}_{10}$, $\mathbf{f}_{01}$, $\mathbf{f}_{11}$ define $\mathbf{f}(0,0)$, $\partial_u \mathbf{f}(0,0)$, $\partial_v \mathbf{f}(0,0)$ and $\partial_u \partial_v \mathbf{f}(0,0)$.

2.2. Geometric continuity

We enforce smoothness as matching of derivatives after change of variables where two surface pieces $\mathbf{f}$ and $\tilde{\mathbf{f}}$ are glued together without overlap: $\mathbf{f}(u,0) = \tilde{\mathbf{f}}(u,0)$. This yields the well-known G^1 constraints

$$\partial_v \tilde{\mathbf{f}} - a(u)\partial_v \mathbf{f} - b(u)\partial_u \mathbf{f} = 0. \quad (1)$$

2.3. Minimizing distortion

If the parameterization of a surface is as uniform as possible, i.e. the first fundamental form of a surface is close to the identity, then functionals such as

$$\mathcal{F}_k f := \int_0^1 \int_0^1 \sum_{i+j=k, i,j \geq 0} \frac{k!}{i!j!}(\partial_s^i \partial_t^j f(s,t))^2 ds dt$$

$$\mathcal{F}_k^* f := \int_0^1 \int_0^1 (\partial_s^k f(s,t))^2 + (\partial_t^k f(s,t))^2 ds dt$$

that act on each coordinate of a surface independently, can be viewed as penalizing deviation from a surface of polynomial degree less than k, see e.g. [HKD93, Gre94, Gre96, LGS99, Sar00, WN01], since polynomials of degree less than k are annihilated by $\mathcal{F}_k$ and polynomials of bi-degree less than k are annihilated by $\mathcal{F}_k^*$.

Penalizing higher-order polynomial terms can be expected to reduce oscillations of the surface. Since our goal is to complete a bi-cubic (bi-3) patch complex by multi-sided caps and since the results of functionals in multi-sided configurations and for non-uniform parameterizations differ strongly from the regular case, it is natural to test and select functionals when the input is the control-net of the characteristic map χ of Catmull-Clark
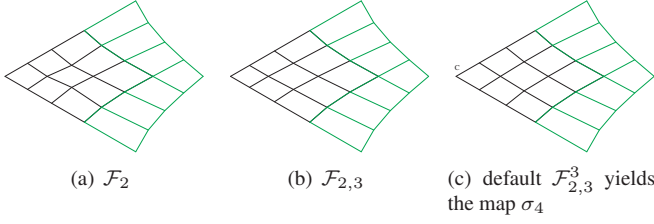
Figure 2: **Characteristic parameterizations** σ when $n = 6$ based on different functionals. Each σ inherits the boundary data (green sub-net) of the Catmull-Clark characteristic map χ.
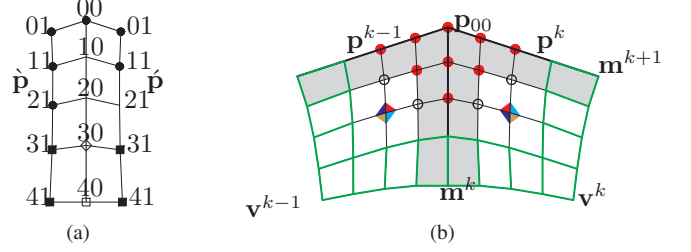

Figure 3: **Bi-4 cap construction.** (a) Labels along the G^1 strip relevant for the G^1 join between adjacent patches; black disks and squares mark BB-coefficients unconstrained after resolving the G^1 constraints in terms of the unmarked BB-coefficients (the asymmetric distribution of marked and unmarked points is no problem since all BB-coefficients together will be set by symmetric constraints). (b) Adjacent bi-4 patches of the cap; green = reparameterized first-order data from **b**. In each sector, the red disks define a quadratic polynomial **q** that, after reparameterization, matches a unique quadratic expansion at $\mathbf{p}_{00}$. This implies a well-defined curvature at $\mathbf{p}_{00}$.

subdivision [Rei93]. For these canonical boundary data, we searched the space with emphasis on the valencies $n = 5, 6$, first applying 'pure' functionals $\mathcal{F}_k$ and $\mathcal{F}_k^*$, $k = 2, \ldots, 4$, and then using linear combinations to optimize the uniformity of the layout of the BB-coefficients surrounding the irregular point. The best combination turned out to be $\mathcal{F}_{2,3}^3 := \mathcal{F}_{2,3}(\mathbf{J}_{0,3}^4 \mathbf{f})$, the restriction of the functional $\mathcal{F}_{2,3} := (3\mathcal{F}_2 + \mathcal{F}_3)/4$ to the 4×4 sub-net $\mathbf{J}_{0,3}^4 \mathbf{f}$ of the BB-net of the bi-4 patch $\mathbf{f}$, interpreted as the BB-net of a bicubic patch (see the black 4×4 sub-nets in Fig. 2).

However, when working in 3-space and blending higher-order data from $n \neq 4$-sided neighborhood of an extraordinary point in a bi-cubic patch complex, the parameterization naturally changes towards that point. This change is all the more rapid when we keep the polynomial degree and the number of patches is low. This may explain why experiments consistently showed that, for setting degrees of freedom of our bi-4 *surface* cap in 3-space, even the best choice $\mathcal{F}_{2,3}^3$ is ultimately worse than approximating a carefully crafted bi-5 guide cap **g** [KP15b] that exploits second-order data of the tensor-border **b** for a gentle propagation of the curvature from the boundary into the cap. We will see evidence of this later in the paper, e.g in Fig. 6h,i and Fig. 8. Therefore $\mathcal{F}_{2,3}^3$ will be used for reparameterizations whereas a guide surface will determine the geometric shape near the irregular point.

3. The G^1 bi-4 cap construction for $n = 5, 6, 7$

In deriving the construction, we first assure pairwise G^1 connection of the n patches into a cap, then connect the cap smoothly to the data, and finally optimize shape.

3.1. G^1 continuity of the cap

We consider two adjacent patches $\grave{\mathbf{p}} := \mathbf{p}^{k-1}$ and $\acute{\mathbf{p}} := \mathbf{p}^k$, $k = 0, \ldots, n-1$ (superscript modulo n) that join along their shared boundary curve $\grave{\mathbf{p}}(u, 0) = \acute{\mathbf{p}}(u, 0)$ (cf. Fig. 3a : locally, for two adjacent patches, it is convenient to index the coefficients symmetric with respect their shared curve rather than rotational symmetric with respect to the irregular point as is appropriate for the full cap in terms of $\mathbf{p}^k$.)

Symmetry of construction forces $a(u) := -1$. Our choice of $b(u)$ is

$$b(u) := 2\mathsf{c}(1-u) , \text{ where } \mathsf{c} := \cos\frac{2\pi}{n} . \qquad (2)$$

Then (1) becomes

$$\partial_v \grave{\mathbf{p}} + \partial_v \acute{\mathbf{p}} = 2\mathsf{c}(1-u)\partial_u \acute{\mathbf{p}}, \qquad (G_|^1)$$

and $(G_|^1)$ is enforced between $\grave{\mathbf{p}}$ and $\acute{\mathbf{p}}$ by setting the BB-coefficients (represented as unmarked points, hollow diamond and hollow square in Fig. 3a) to

$$\grave{\mathbf{p}}_{10} := \left(1 - \frac{1}{\mathsf{c}}\right)\grave{\mathbf{p}}_{00} + \frac{\grave{\mathbf{p}}_{01} + \acute{\mathbf{p}}_{01}}{2\mathsf{c}}; \qquad (3)$$

$$\grave{\mathbf{p}}_{20} := \frac{(3\mathsf{c} - 4)\grave{\mathbf{p}}_{10} + 2(\grave{\mathbf{p}}_{11} + \acute{\mathbf{p}}_{11})}{3\mathsf{c}}; \qquad (4)$$

$$\acute{\mathbf{p}}_{21} := (2 - \mathsf{c})\grave{\mathbf{p}}_{20} + \mathsf{c}\grave{\mathbf{p}}_{30} - \grave{\mathbf{p}}_{21}; \qquad (5)$$

$$\grave{\mathbf{p}}_{30} := \frac{2(\grave{\mathbf{p}}_{31} + \acute{\mathbf{p}}_{31}) - \mathsf{c}\grave{\mathbf{p}}_{40}}{4 - \mathsf{c}} ; \qquad (6)$$

$$\grave{\mathbf{p}}_{40} := \frac{\grave{\mathbf{p}}_{41} + \acute{\mathbf{p}}_{41}}{2}. \qquad (7)$$

All the other BB-coefficients (marked as black disks and squares in Fig. 3a) remain unconstrained in this solution *local* to two adjacent patches. To obtain tangent continuity at the irregular point, we use (3) and re-express all but two of the tangent coefficients recursively as $\acute{\mathbf{p}}_{01} := 2(1 - \mathsf{c})\grave{\mathbf{p}}_{00} + 2\mathsf{c}\grave{\mathbf{p}}_{10} - \grave{\mathbf{p}}_{01}$.

3.2. G^1 join with the tensor-border **b**

Equation (7) is due to the fact that the pieces of **b** are smoothly connected splines. By contrast, (6) does not directly equate derivatives. The tensor-border **b** of depth 1 (the green layers in Fig. 1b) needs to be reparameterized by a map β in order to make these layers consistent with the G^1-strip.

The reparameterization $\beta := (u + b(u)v, a(u)v)$ (see Fig. 4)

$$a(u) := 1 - u + \frac{1}{1 - \mathsf{c}}u , \ b(u) := \frac{\mathsf{c}}{1 - \mathsf{c}}(1 - u)u. \qquad (8)$$

is symmetric with respect to the diagonal $u = v$ and maps β_{00} to $\mathbf{v}^{k-1}$. From (8) we get that the BB-coefficients β_{i0}, $i = 0, 1, 2$, of β represent an identity map in degree-raised form and that

$$\beta_{11} := \left(\frac{2 - \mathsf{c}}{4(1 - \mathsf{c})}, \frac{2 - \mathsf{c}}{4(1 - \mathsf{c})}\right), \ \beta_{21} := \left(1, \frac{1}{2(1 - \mathsf{c})}\right).$$

3

(a) $n = 5$ (b) $n = 6$
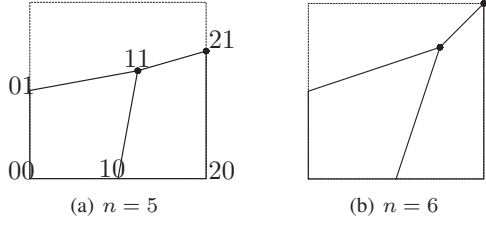
Figure 4: Two layers of BB-coefficients of the **reparameterization** β along one edge (β is symmetric with respect to the diagonal β_{00}, β_{11}).

Since the boundary is the degree-raised input boundary, only the following formulas are required (cf. Fig. 5):

$$\mathbf{p}_{11} := \frac{(1-7\mathsf{c})\mathbf{b}_{00} + 3(\mathbf{b}_{10} + \mathbf{b}_{01}) + 9(1-\mathsf{c})\mathbf{b}_{11}}{16(1-\mathsf{c})},$$

$$\mathbf{p}_{21} := \frac{(1-6\mathsf{c})\mathbf{b}_{10} + (1+\mathsf{c})\mathbf{b}_{20} + 3\mathbf{b}_{11} + 3(1-\mathsf{c})\mathbf{b}_{21}}{8(1-\mathsf{c})},$$

$$\mathbf{p}_{31} := \frac{(3-15\mathsf{c})\mathbf{b}_{20} + (1+2\mathsf{c})\mathbf{b}_{30} + 9\mathbf{b}_{21} + 3(1-\mathsf{c})\mathbf{b}_{31}}{16(1-\mathsf{c})},$$

$$\mathbf{p}_{41} := \frac{(1-4\mathsf{c})\mathbf{b}_{30} + 3\mathbf{b}_{31}}{4(1-\mathsf{c})},$$

where $\mathbf{b}_{ij}$ are the BB-coefficients of input tensor-border $\mathbf{b}$.

(a) input: $\mathbf{b}$ of degree 3   (b) output: $\mathbf{b} \circ \beta$ of degree 4
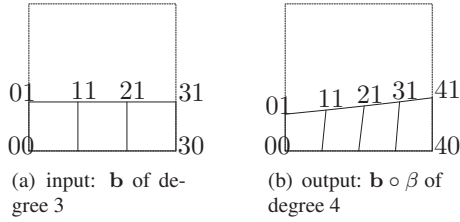
Figure 5: Indices of (a) the input **tensor-border** $\mathbf{b}$ of degree 3 and of (b) the reparameterized data $\mathbf{b} \circ \beta$ of degree 4.

3.3. Construction via a bi-5 guide

The denominator term $(1-\mathsf{c})$ in formula (8) hints at instability and distortion as the valence n increases. Indeed, already for $n = 6$, Fig. 4b the reparameterization β is quite non-uniform. Fig. 6b,d,h illustrate that bi-4 constructions that set the remaining $2 + 3n$ coefficients by minimizing functionals, fail to yield good highlight lines, even when the irregular point is set to the central limit point of Catmull-Clark subdivision (if not, the results are worse). In particular, the standard functional $\mathcal{F}_2^*$ fares poorly.

We therefore stabilize the construction by approximating a reference surface. The cap construction $\mathbf{g}$ of [KP15b] is G^2 at the irregular point and joins G^1 with the tensor-border data, capturing also second-order data from the tensor-border. It generates consistently high-quality highlight lines. However, directly transferring jets of the bi-5 guide $\mathbf{g}$ yields poor highlight lines: the bi-4 surface and the bi-5 reference surface must be carefully related. Let σ_4 be the map constructed in Section 2.3 (see Fig. 2c) and σ_5 the map constructed by [KP15b] when the characteristic map χ of Catmull-Clark subdivision provides the

(a) $n = 6$ CC-net   (b) $\mathcal{F}_2^*$ (c) [LSNC09]

(d) $\mathcal{F}_{2,3}^3$ (e) this paper   (f) Catmull-Clark

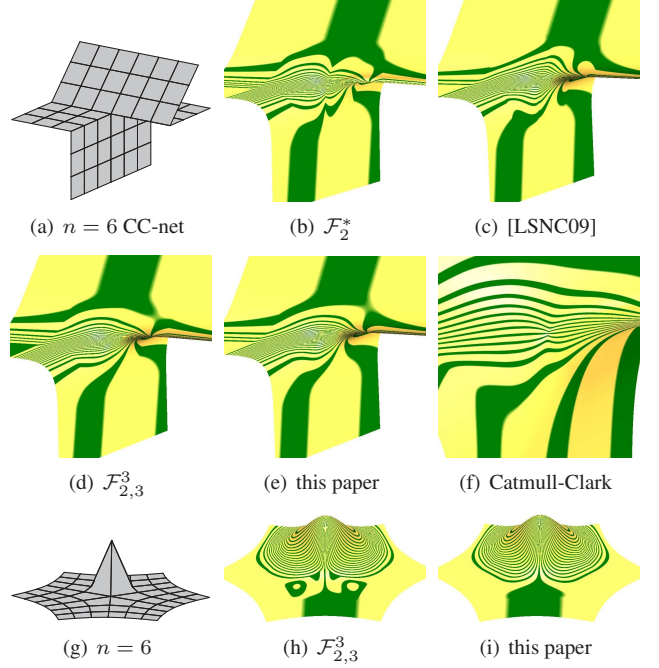(g) $n = 6$ (h) $\mathcal{F}_{2,3}^3$ (i) this paper

Figure 6: The effect of various **functionals and the reparameterization** of a guide surface on the highlight line distribution [BC94]. Clearly, the surfaces (b) that minimize $\mathcal{F}_2^*$, the construction (c) of [LSNC09] and (f) Catmull-Clark subdivision do not yield acceptable quality. While $\mathcal{F}_{2,3}^3$ does well on (a), comparison of (h) and (i) for input (g) shows it to be inferior to our more complex bi-5 guided approach.

tensor-border data. We generate an intermediate bi-4 patch $\mathbf{a}$ from the jets at the corner points $\mathbf{s}$ of the reparameterized construction $\mathbf{g}$ (see Fig. 7c) as

$$\mathbf{J}_{\mathbf{s},2}^4 \mathbf{a} := \mathbf{J}_{\mathbf{s},2}^4(\mathbf{g} \circ \sigma_5^{-1} \circ \sigma_4). \quad (9)$$

Then, as indicated in Fig. 7d, we average some coefficients that overlap. Let $\mathbf{q}$ be the unique quadratic (expansion) at $\mathbf{s} := \mathbf{p}_{00}$. Since the circled BB-coefficients of $\mathbf{g}$ in Fig. 7a are part of $\mathbf{J}_{\mathbf{s},2}^5(\mathbf{q} \circ \sigma_5)$,

$$\mathbf{J}_{\mathbf{s},2}^4 \mathbf{a} = \mathbf{J}_{\mathbf{s},2}^4((\mathbf{q} \circ \sigma_5) \circ \sigma_5^{-1} \circ \sigma_4) = \mathbf{J}_{\mathbf{s},2}^4(\mathbf{q} \circ \sigma_4).$$

That is, the coefficients marked as red disks in Fig. 7d stem from $\mathbf{J}_{\mathbf{s},2}^4(\mathbf{q} \circ \sigma_4)$ and the bi-4 surface is *curvature continuous* at the irregular point! Since the BB-coefficients of σ_4 satisfy (3), (4) it is easy to check that so do the BB-coefficients of $\mathbf{J}_{\mathbf{s},2}^4(\mathbf{q} \circ \sigma_4)$. And since we retain the tensor-border (green disks in Fig. 7d) to guarantee the G^1 join with the tensor-border, also (6) and (7) hold. Additionally enforcing (5) leaves unconstrained only the n BB-coefficients $\grave{\mathbf{p}}_{21}^k$. These points we fix by minimizing the sum of squared distances between coefficients of $\mathbf{a}$ and $\mathbf{p}$ (circled points in Fig. 3b):

$$\min_{\{\grave{\mathbf{p}}_{21}^k\}} \sum_{k=0}^{n-1} \|\mathbf{p}_{ij}^k - \mathbf{a}_{ij}^k\|^2, \quad ij \in \{12, 21\}. \quad (10)$$

Now, thanks to referencing a high-quality, higher-degree surface, we obtain good bi-4 caps for $n = 6$, Fig. 8 and even for $n = 7$ Fig. 9.
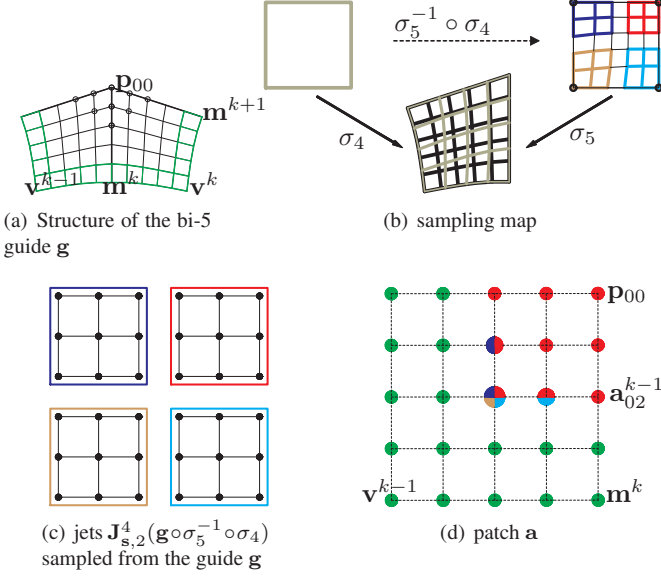
(a) Structure of the bi-5 guide $\mathbf{g}$

(b) sampling map

(c) jets $\mathbf{J}_{\mathbf{s},2}^4(\mathbf{g}\circ\sigma_5^{-1}\circ\sigma_4)$ sampled from the guide $\mathbf{g}$

(d) patch $\mathbf{a}$

Figure 7: **Guide-based construction.** Note in (d) that $\mathbf{a}_{02}^{k-1}$ and its symmetric counterpart are taken exclusively from the jet at $\mathbf{p}_{00}$ of the bi-5 guide and so ensures G^2 continuity at $\mathbf{p}_{00}$.
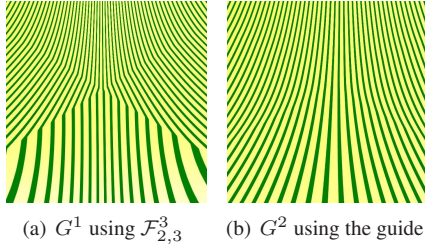

(a) G^1 using $\mathcal{F}_{2,3}^3$

(b) G^2 using the guide

Figure 8: Rendering just the cap (for input Fig. 6g) demonstrates the advantage of (b) **enforcing $\mathbf{G^2}$ continuity at the irregular point** in the new bi-4 construction over (a) the G^1 $\mathcal{F}_{2,3}^3$-based construction.

3.4. Implementation via generating functions

The construction via sampling a guide surface seems unduly cumbersome. However, due to the relatively short, explicit formulas (3)–(7) for the dependent BB-coefficients in terms of the independent BB-coefficients, most of the construction steps are simple and all are explicit and stable. The minimization (10) yields a linear system of size $n \times n$ that, since the guide is fixed, is solved for each unknown separately once and for all. For $5, 6, 7$, we can therefore compute and tabulate the seven *generating functions of the CC-net*. The final surface cap is a linear combination of these tabulated generating functions, weighted by their CC-net points.

Specifically, since the algorithm works for each coordinate separately, it can be applied when all CC-net points $\mathbf{c}_m$ have value 0, except for $\mathbf{c}_m^0 = 1$, for one of $m = 1, \ldots, 7$ (see Fig. 1a). This yields the scalar-valued bi-4 coefficients

$$h_{ij}^{k,m} \in \mathbb{R}, \quad k = 0, \ldots, n-1, \, m = 1, \ldots, 7, \, i,j \in \{0, \ldots, 4\},$$

where $h_{ij}^{0,7} = \ldots = h_{ij}^{n-1,7}$. Then the BB-coefficients of the

patch covering sector κ are

$$\mathbf{p}_{ij}^{\kappa} := h_{ij}^{0,7}\mathbf{c}_7^0 + \sum_{k=0}^{n-1}\sum_{m=1}^{6} h_{ij}^{k,m}\mathbf{c}_m^{\kappa-k}, \tag{11}$$

where the superscript of $\mathbf{c}_m^{\kappa-k}$ is interpreted modulo n. Almost two thirds of the BB-coefficients of each patch is determined by the simple formulas of $\mathbf{b} \circ \beta$ in (3.2). Only $\mathbf{J}_{0,2}^4\mathbf{p}$, i.e. the 2×2 sub-nets at the irregular point, needs to be tabulated to construct a cap or to assemble IGA stiffness matrices.

(a) $n = 7$

(b) this paper

(c) $\mathcal{F}_{2,3}^3$

(d) bi-5 guide

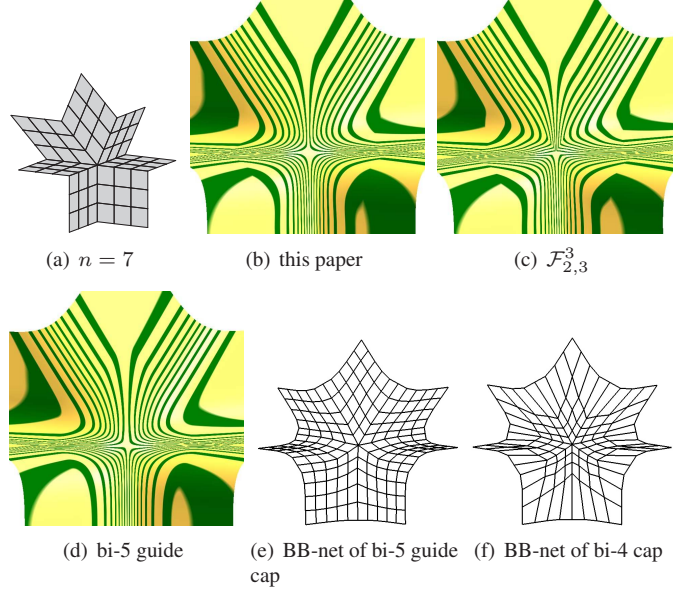(e) BB-net of bi-5 guide cap

(f) BB-net of bi-4 cap

Figure 9: Highlight lines for a saddle with **valence 7** show (b) the (curvature continuous at the irregular point) new bi-4 construction to be of higher quality than (c) the best choice of the functional minimization approach. The new bi-4 construction is of quality comparable to (d) its bi-5 guide [KP15b] – despite the far more uneven BB-net: (f) vs. (e).
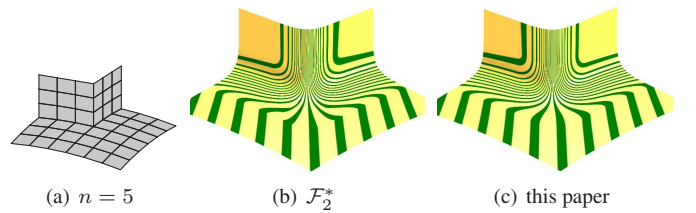

(a) $n = 5$

(b) $\mathcal{F}_2^*$

(c) this paper

Figure 10: $\mathcal{F}_2^*$ **fails** to yield smooth highlight lines already for $n = 5$.

3.5. Examples and comparison of caps when $n \in \{5, 6, 7\}$

To stress-test the construction, we concentrate on small CC-nets that challenge the constructions and reveal their flaws.

Fig. 9c shows that, even when $n = 7$, the highlight lines of the new bi-4 construction with curvature continuity at the irregular point are better distributed than those for the best functional $\mathcal{F}_{2,3}^3$ that is everywhere only G^1. By contrast, Fig. 10 shows failure of the standard functional $\mathcal{F}_2^*$ to generate satisfactory highlight lines already for $n = 5$.
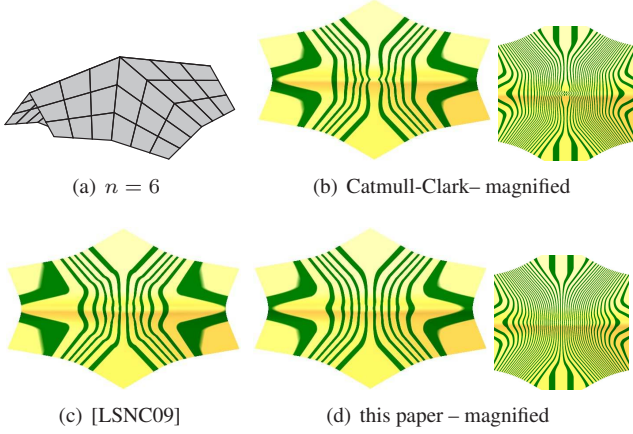
5

(a) $n = 6$ (b) Catmull-Clark– magnified

(c) [LSNC09]   (d) this paper – magnified

Figure 11: **Convexity** preservation or lack thereof for a paraboloid-like CC-net.

(a) input design sketch   (b) CC-net

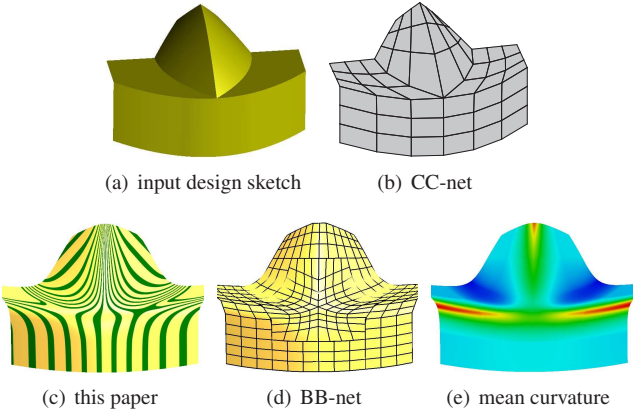(c) this paper   (d) BB-net   (e) mean curvature

Figure 12: A **design sketch** (a), consisting of five primitive surfaces, is (b) approximated by a CC-net of valence $n = 6$ and converted into a bi-4 surface (c).

(a) input **b**   (b) BB-net

Figure 13: **Indexing when n = 3**. The disks define the irregular point and its tangent plane. The mesh of $\mathbf{b} \circ \beta$ is shown in green.

(a) CC-net   (b) G^2 bi-7   (c) G^1 bi-4

(d) CC-net   (e) G^2 bi-7   (f) G^1 bi-4

(g) G^2 bi-7   (h) G^1 bi-4

Figure 14: **n = 3**-sided caps. Comparison of G^1 bi-4 (this paper) with G^2 bi-7 [LS08]. (b,c) compare Gauss curvature, (e,f) mean curvature and (g,h) highlight shading.

Fig. 11 tests the convexity preservation of the bi-4 construction. Catmull-Clark subdivision, although C^2 everywhere apart the irregular point, shows poorer highlight lines than the new bi-4 construction. Typically Catmull-Clark subdivision does well across the border but pays the price near the irregular point: the surface oscillates in its vicinity. The effort of the new bi-4 construction in transitioning also yields better highlight lines than the Gregory patch construction [LSNC09] (whose highlight lines at the irregular point are better distributed than those of Catmull-Clark subdivision). [LSNC09] allows quads to have more than one vertex is of valence $n \neq 4$, but typically to the detriment of shape.

Fig. 12 represents a design ensemble of basic primitive surfaces. The initial sketch Fig. 12a is re-approximated in (b) by a CC-net such that moving the primitives corresponds to moving blocks of B-spline control points. Even though the input is challenging, the mean curvature of the resulting G^1 bi-4 surface is acceptable, e.g. without oscillations.
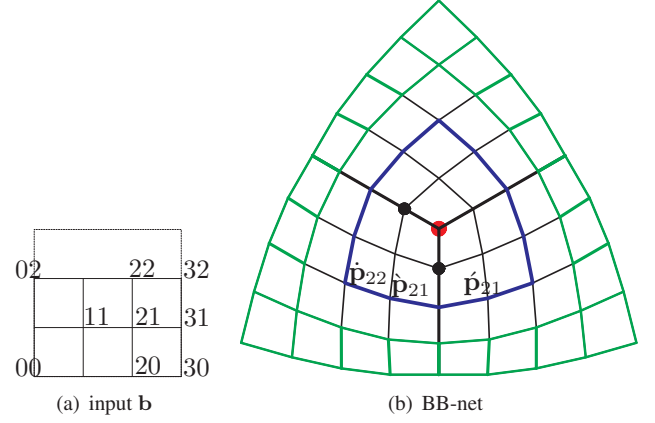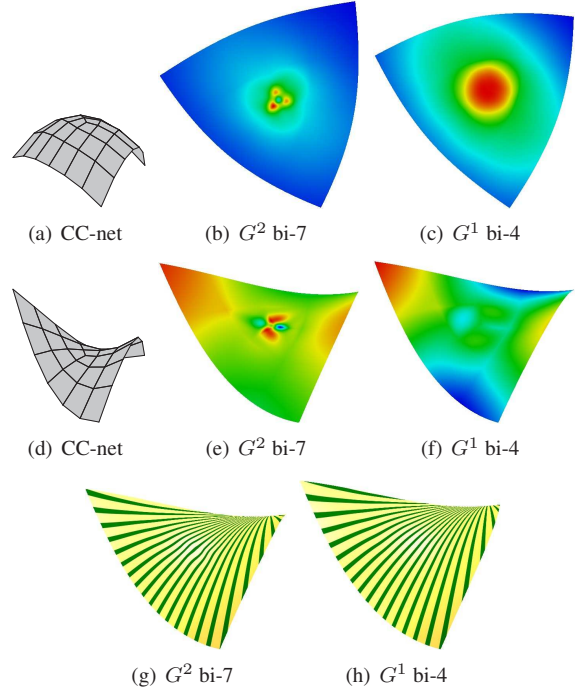
4. Construction when valence $n = 3$

With the notation of Fig. 13, we write (5) as

$$\grave{\mathbf{p}}_{20} := \frac{2}{5}(\grave{\mathbf{p}}_{21} + \acute{\mathbf{p}}_{21}) + \frac{1}{5}\grave{\mathbf{p}}_{30} \text{ , implying that (4) becomes}$$

$$4(\grave{\mathbf{p}}_{11} + \acute{\mathbf{p}}_{11}) - 11\grave{\mathbf{p}}_{10} + 3\grave{\mathbf{p}}_{20} = 0 \text{ .} \tag{12}$$

The 3×3 system of linear equations of type (12) in the unknowns $\mathbf{p}_{11}^k$, $k = 0, 1, 2$, has a unique solution. With $\mathbf{b}_{ij}$ the BB-coefficients of the input tensor-border $\mathbf{b}$, labeled as shown in Fig. 13a, we derive, following the process laid out

in [KP15b],

$$\dot{\mathbf{p}}_{21} := \sum_{i=2}^{3}\sum_{j=0}^{2} e_{ij}\mathbf{b}_{ij}\,, \quad \dot{\mathbf{p}}_{22} := \sum_{i=0}^{2}\sum_{j=0}^{2} \dot{e}_{ij}\mathbf{b}_{ij}\,,$$

$$e_{20} := \frac{13}{144},\ e_{30} := -\frac{3}{40},\ e_{21} := \frac{7}{12},$$

$$e_{31} := \frac{89}{720},\ e_{22} := \frac{1}{6},\ e_{32} := \frac{1}{9}\,;$$

$$\dot{e}_{00} := \frac{7}{540},\ \dot{e}_{11} := \frac{11}{18},\ \dot{e}_{22} := \frac{1}{4},\ \dot{e}_{10} := -\frac{4}{135},$$

$$\dot{e}_{20} := \frac{1}{108},\ \dot{e}_{21} := \frac{1}{12},\ \dot{e}_{ji} = \dot{e}_{ij}.$$

The BB-coefficient $\acute{\mathbf{p}}^{21}$ is defined symmetrically and the irregular point is defined as

$$(1 - 3\gamma_5 - 3\gamma_6)\mathbf{c}_7^0 + \sum_{i=0}^{3}(\gamma_5\mathbf{c}_5^i + \gamma_6\mathbf{c}_6^i), \quad \gamma_5 := \frac{5}{96},\ \gamma_6 := \frac{1}{6}\,.$$

(the choice of such weights has been detailed in [KP15b]). The remaining two free points (black disks in Fig. 13b) are fixed by minimizing $\sum_{k=0}^{2}\mathcal{F}_4\mathbf{p}^k$.

Fig. 14 shows this solution to be of high quality, better than the G^2 scheme of degree bi-7 in [LS08]: for $n = 3$, higher continuity everywhere does not seem necessary for good highlight lines or curvature distribution (the new cap is curvature continuous at the irregular point).

5. Caps for high valences

In practice, valences $n > 7$ are uncommon and usually a construction for $n \in \{3, 4, 5, 6\}$ suffices. For $n = 7$, the BB-net of the new bi-4 cap starts to be very non-uniformly distributed and for configurations such as Fig. 9a, the surface quality deteriorates after one Catmull-Clark step. This is unusual since a single refinement step is typically beneficial as it softens transitions. Since we do not want to rule out valencies $n > 7$, we briefly develop G^1 caps of good quality, consisting from 2×2 bi-4 macro-patches; and we also sketch an alternative construction that is 'almost' G^1.

5.1. G^1 2×2 bi-4 caps

The 2×2 macro-patch construction, illustrated in Fig. 15a,b, transitions G^1 across the tensor-border $\mathbf{b}$. That is, the data are reparameterized immediately – as opposed to more classical constructions that connect C^1 to the tensor-border data and C^1 to innermost subpatches (see Fig. 15c). For low degree constructions such C^1 prolongations are known to result in considerably poorer quality despite formally an equal set of degrees of freedom (the degrees of freedom can be visualized in Fig. 15b vs. Fig. 15c).

We ensure G^1 continuity between the central sub-patches $\grave{\mathbf{p}}$ and $\acute{\mathbf{p}}$ by enforcing

$$\grave{\mathbf{p}}_v + \acute{\mathbf{p}}_v = (2(1 - u) + \gamma u)\mathsf{c}\grave{\mathbf{p}}_u, \quad \mathsf{c} := \cos\frac{2\pi}{n}, \quad (13)$$
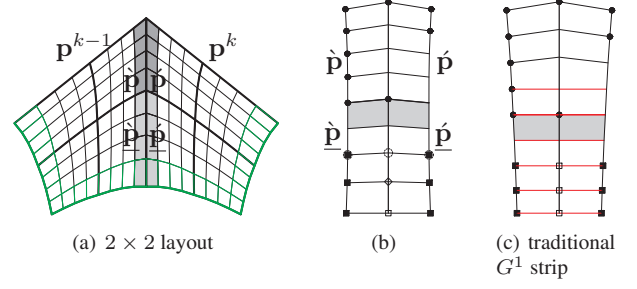

(a) 2×2 layout　　(b)　　(c) traditional G^1 strip

Figure 15: Layout of the **2×2 macro-patches** when $n > 6$. In (a), the **G^1 strip** of BB-coefficients involved in the G^1 constraints between the macro-patches is underlaid in gray. In (b) and (c) the degrees of freedom after enforcing G^1 continuity are indicated as black boxes ■ and black disks ●. (b) shows our G^1 strip while (c) shows the commonly-used strip, where the border data are extended C^1.

(a) $n = 5$　(b) C^1 prolongation　(c) G^1 prolongation

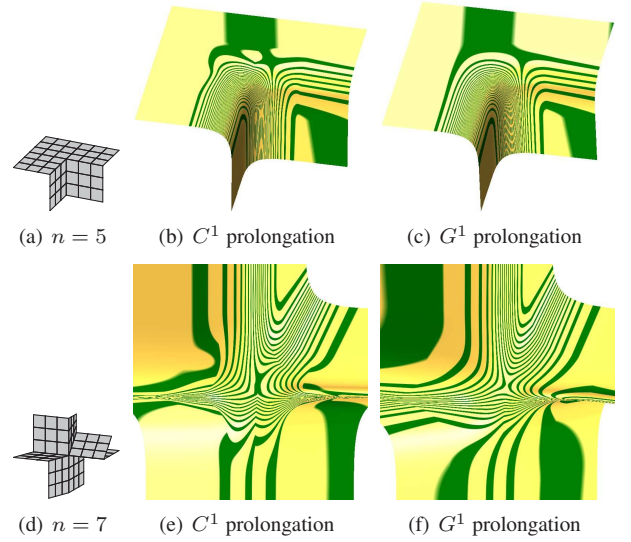(d) $n = 7$　(e) C^1 prolongation　(f) G^1 prolongation

Figure 16: The **advantage of G^1 prolongation** of the tensor-border data. (c) is the single patch per sector construction of Section 3 and (f) the 2×2 construction for higher valences, (b) and (e) are alternative but inferior 2×2 bi-4 construction variants that extend the tensor-border without reparameterization.

(a) $n = 8$　　(b) [LS08]

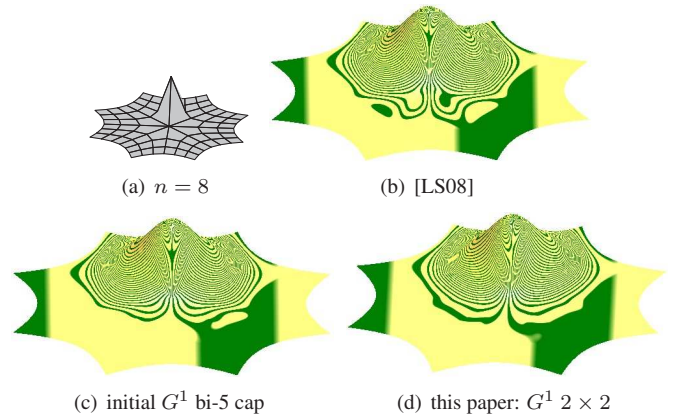(c) initial G^1 bi-5 cap　　(d) this paper: G^1 2×2

Figure 17: **$G^1 2 \times 2$** bi-4 construction yields a highlight line distribution competitive with the bi-7 construction in [LS08] and the bi-5 guide surface.

and between border sub-patches $\underline{\grave{\mathbf{p}}}$ and $\underline{\acute{\mathbf{p}}}$ by enforcing

$$\underline{\grave{\mathbf{p}}}_v + \underline{\acute{\mathbf{p}}}_v = \gamma(1 - u)\mathsf{c}\underline{\grave{\mathbf{p}}}_u, \quad \gamma^{def} := 1.13 - 0.9\mathsf{c} + 0.36\mathsf{c}^2 \quad (14)$$

7

where the coefficients underlaid in grey in Fig. 15b are determined by C^1-extension of $\grave{\mathbf{p}}$ and $\acute{\mathbf{p}}$. The BB-coefficients unconstrained after enforcing the G^1 constraints are marked as the black disks and black quads in Fig. 15b. The part of the control net of the sub-patches $\underline{\grave{\mathbf{p}}}$ and $\underline{\acute{\mathbf{p}}}$ rendered green in Fig. 15a matches the reparameterized and subsequently split tensor-border $\mathbf{b}$. The border reparameterization with functions

$$a(u) := \frac{1 - \gamma\mathsf{c}(1-u)}{1 - \gamma\mathsf{c}}, \; b(u) := \frac{\gamma\mathsf{c}(1-u)u}{1 - \gamma\mathsf{c}}, \qquad (15)$$

generalizes (8). (In (8), $\gamma := 1$.) Our choice γ^{def} prevents the high distortion of reparameterized tensor-border $\mathbf{b}$, that limited the single-patch bi-4 construction to $n \leq 7$.

To set the remaining degrees of freedom is non-trivial: functionals failed even more egregiously than in the single-patch case. Numerous experiments confirm as a good strategy to reduce to degree 3 some layers of the bi-4 macro patches, by applying the constraint pattern

$$\mathbf{p}_2 := \frac{2}{3}(\mathbf{p}_1 + \mathbf{p}_3) - \frac{1}{6}(\mathbf{p}_0 + \mathbf{p}_4). \qquad (16)$$

For example, in Fig. 15b, two circled markers are set by (16) implying that the third also satisfies (16). The remaining construction is analogous, but more complex than that of Section 3: the details of inheriting data from the guide map via a careful reparameterization are explained in Appendix A.

Fig. 16 and Fig. 17 give an impression of the good highlight line distribution of the resulting 2×2 cap of degree bi-4. The data of Fig. 16d in particular, rule out fitting the neighborhood of the irregular point with a single polynomial of low degree as would be needed to deploy the low-degree (bi-6) versions of [Pra97, Rei98, Lev06].

5.2. An almost G^1 bi-4 cap

As a structurally simpler alternative to the 2×2 construction, we sketch almost-G^1 bi-4 caps with the same layout of n patches as the main construction of Section 3. Here *almost* refers to *small* discontinuities of the normal across the tensor-border. Whereas deriving surfaces by leaving out smoothness constraints typically yields poor highlight lines, our almost-G^1 caps are based on [KP15b]. The jets $\mathbf{J}_{\mathbf{s},2}^5 \mathbf{f}$ of the construction [KP15b] (see Fig. 18a) are converted to $\mathbf{J}_{\mathbf{s},2}^4 \mathbf{f}$ and averaged at some overlapping locations as shown in Fig. 18b, yielding an auxiliary bi-4 cap $\mathbf{a}$. Arguments as in Section 3 show $\mathbf{a}$ to be curvature continuous at the irregular point and prove that the bi-4 cap $\mathbf{a}$ satisfies the G^1 constraints (3), (4), (6), (7), but not necessarily (5).

The remaining BB-coefficients are fixed by minimizing (10). Given [KP15b], the derivation of the generating functions is considerably simpler than those of the G^1 2×2 cap. At runtime, working with the tabulated generating functions, there is little difference in the complexity.

The almost G^1 bi-4 cap is internally G^1-connected but formally only G^0-connected to the degree 3 tensor-border. Experiments consistently show a deviation of the normal of less than $0.1°$ so that the surfaces look smooth by industrial standards

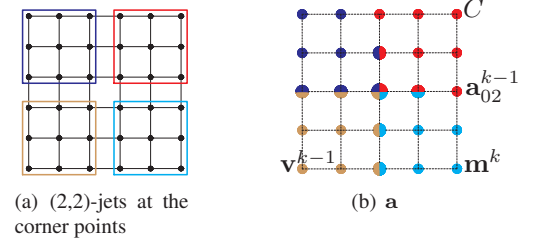(a) (2,2)-jets at the corner points

(b) $\mathbf{a}$

Figure 18: **Approximate bi-4 cap construction**. (a) Bi-5 patch as a collection of four (2,2)-jets. (b) Auxiliary bi-4 patch obtained by (2,2)-jets, averaging some where they overlap. Note that $\mathbf{a}_{02}^{k-1}$ and its symmetric counterpart are taken exclusively from the central jet to ensure G^2 continuity at $\mathbf{p}_{00}$.

(a) $n = 8$, design sketch

(b) CC-net

(c) initial G^1 bi-5 cap

(d) almost G^1 bi-4
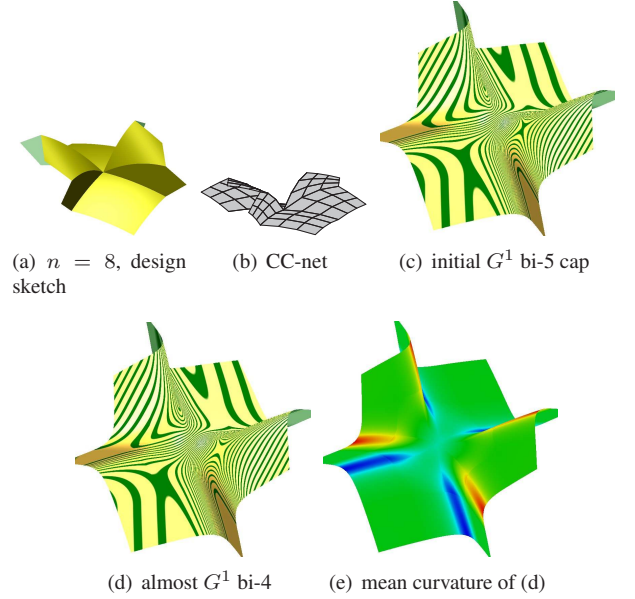
(e) mean curvature of (d)

Figure 19: Challenging configuration resulting from a design controlled by a collection of basic surfaces.

[Tut15]. For some challenging high-valence configurations violate the $0.1°$ bound and this is visible under scrutiny, e.g. in Fig. 20e. One Catmull-Clark refinement step typically enforces the angle bound so that the surface looks G^1 with good highlight line distribution, even under magnification.
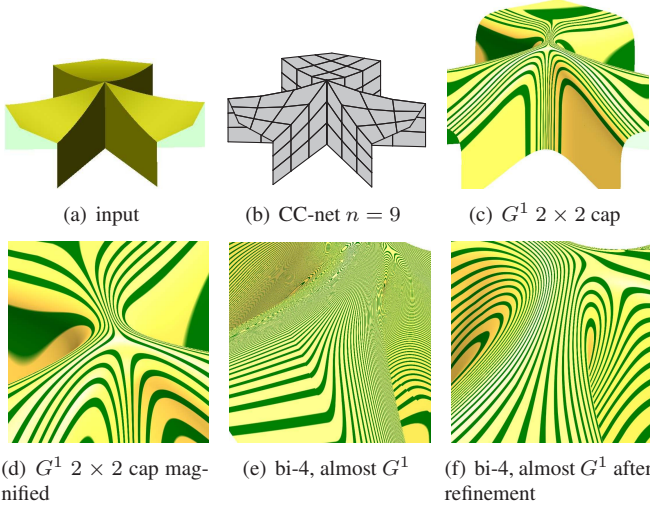
(a) input

(b) CC-net $n = 9$

(c) G^1 2×2 cap

(d) G^1 2×2 cap magnified

(e) bi-4, almost G^1

(f) bi-4, almost G^1 after refinement

Figure 20: **High valence**. Based on the CC-net-approximation (bb) of a collection of simple surfaces (a), the 2×2 macro-patch cap shown in (c) and (d) shows a good highlight line distribution also for $n = 9$. Zooming in on the 'almost' G^1 construction betrays a slight the normal discrepancy of $\approx 0.13°$. After one CC-refinement (f), the deviation is reduced to $\approx 0.02°$, i.e. looks G^1 even after magnification.

(a) $n = 5$

(b) $n = 7$

(c) $n = 5$

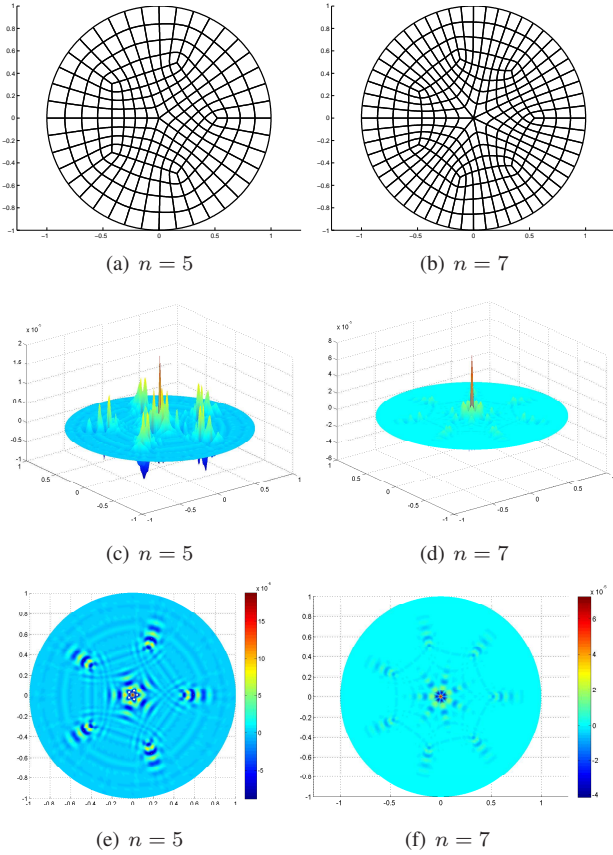(d) $n = 7$

(e) $n = 5$

(f) $n = 7$

Figure 21: **Poisson's equation on the disk**. (a,b) input meshes. (c,d,e,f) error distribution.

6. Isogeometric Analysis

Analogous to the geometric obstacle course (see [KP15c] for data), we now test the new construction on a finite element obstacle course. That is, we test the new bi-4 construction as generalized IGA element on a set of standard problems: Poisson's equation on the disk and Koiter's thin-shell analysis as part of the shell obstacle course. Here both the physical domain X and the analysis functions u_k (e.g. measuring displacement) are represented as a linear combination of the G^1 generating functions $h^{k,m}$ of (11). We form N generalized IGA elements $u_k \circ \mathbf{x}_k^{-1} : X \to \mathbb{R}$, $k = 1, \ldots, N$, where N is the number of CC-net control points $\mathbf{c}_k$ and the physical domain manifold X is assembled as a superposition of maps $\mathbf{x}_k$ that are generating functions weighted by $\mathbf{c}_k$. Since both u_k and $\mathbf{x}_k$ are G^1 with the same reparameterization, C^1 continuity of the generalized IGA elements across irregular points is guaranteed according to [GP15].

Since the exact solution of Poisson's Equation

$$\text{find } u : X \to \mathbb{R} : \begin{cases} -\Delta u = f & \text{in } X, \\ u = 0 & \text{on } \partial\Omega, \end{cases} \quad (17)$$

is well-known, we can plot the error in the finite element approximations for various refinements of the input mesh (see Fig. 21 for two valences; the circular boundary is captured exactly as a rational quadratic). For the input mesh Fig. 21a, the graphs Fig. 22 compare the error convergence of the generalized IGA element built from the single-patch-per-quad bi-4 construction of this paper, the bi-5 elements of [NKP14] and an element built from [KP14]. As expected, the increased degree of the bi-5 elements yields a lower error and the lower degree of the elements from [KP14] a higher error than our new bi-4 elements. The L^2 convergence rate however, is comparable. In the same graph, but for the input mesh of valence $n = 7$ of Fig. 21b, we compare the single patch bi-4 construction to the 2×2 bi-4 construction. Again the more complex construction has a slightly lower overall error. In all cases the L^2 convergence is slightly higher than $O(h^3)$ and the L^∞ convergence is slightly higher than $O(h^2)$ ([KP14] actually achieves a rate of $O(h^3)$ but its L^∞ error is higher overall). The L^∞ error distribution at the first refinement is shown in Fig. 21c,d and, again in Fig. 21e,f. Unsurprisingly, the error is maximal at the irregular points.

Poisson's Equation – generalized IGA element from this paper						
	L^2		L^∞		H^1	
ℓ	$||u - u_h||$	c.r.	$||u - u_h||$	c.r.	$||u - u_h||$	c.r.
1	1.8408e-5	-	7.8945e-5	-	0.0007	-
2	2.1432e-6	8.56	1.8145e-5	4.35	0.00016	4.45
3	2.0895e-7	10.26	4.2639e-6	4.26	3.4313e-5	4.76
4	2.2643e-8	9.23	9.9946e-7	4.27	7.7870e-6	4.41
5	2.5179e-9	9.00	2.3400e-7	4.27	1.8006e-6	4.32

Table 1: Numerical tabulation of the error and the convergence rate (c.r.) of the elements built from the bi-4 construction of this paper – for Poisson's equation on the disk.

Next, we analyze two instances of Koiter's shell model [Koi70] based on Kirchhoff-Love assumptions that lines nor-
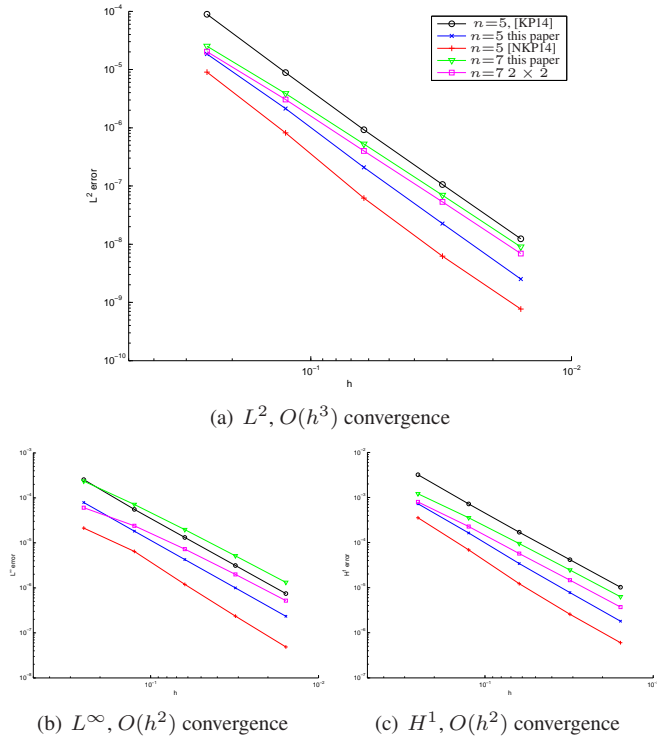
(a) L^2, $O(h^3)$ convergence

(b) L^∞, $O(h^2)$ convergence

(c) H^1, $O(h^2)$ convergence

Figure 22: **Error convergence** of Poisson's equation under mesh refinement.

(a) input mesh

(b) x-displacement

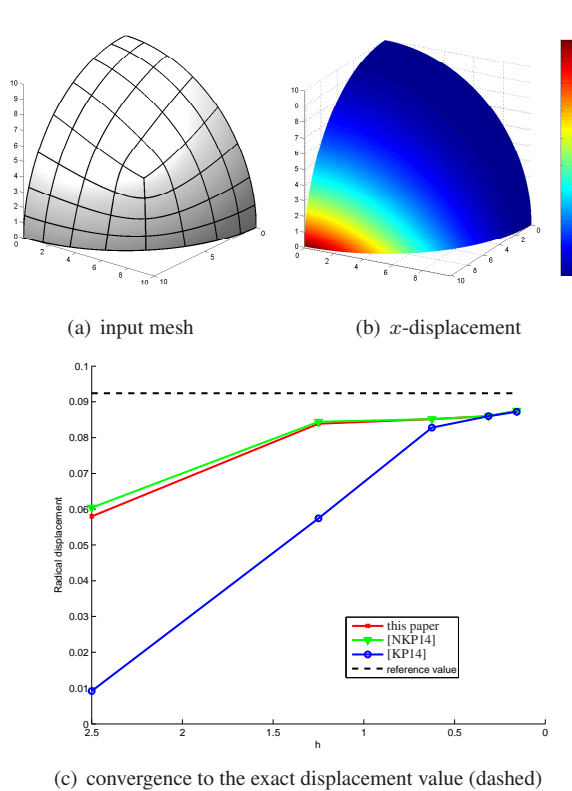(c) convergence to the exact displacement value (dashed)

Figure 23: Octant of a spherical shell. The dashed line in (c) indicates the exact radial displacement at the load point (red in (b)).

mal to the 'middle surface' in the original configuration $\bar{\mathbf{x}}$ remain normal to the middle surface in the deformed configu-

ration $\mathbf{x}$, and that there is no transverse shear strain and stress. The displacement vector field $\mathbf{u}(\theta_1, \theta_2) = \mathbf{x}(\theta_1, \theta_2) - \bar{\mathbf{x}}(\theta_1, \theta_2)$ of the thin shell is found by minimizing the total potential energy function

$$\Pi(\mathbf{u}) = \int_\Omega \left(\frac{Eh}{1-\nu^2} \alpha^T \mathbf{H}\alpha + \frac{Eh^3}{12(1-\nu^2)} \beta^T \mathbf{H}\beta \right) d\Omega \quad (18)$$
$$- \int_\Omega \mathbf{u}^T \mathbf{b} d\Omega - \int_{\Gamma_t} \mathbf{u}^T \mathbf{t} d\Gamma,$$

where $\mathbf{b}$ is the body force, $\mathbf{t}$ is the traction on some parts Γ_t of the shell, $\alpha_{ij} + \theta_3 \beta_{ij}$ is the Green-Lagrange strain tensor, $\mathbf{H}$ is a 3×3 matrix incorporating the metric, and E and ν are the Young modulus and Poisson's ratio, respectively.

Both the sphere-under-load and the Scordelis-Lo roof benchmark problem of the shell obstacle course [BSL+85] are modeled as $(a(x,y), b(x,y), c(x,y))$ where the map $(x,y) : \mathbb{R}^2 \to \mathbb{R}^2$ is constructed by our algorithm while the maps $a, b, c : \mathbb{R}^2 \to \mathbb{R}$ are analytical functions.

Fig. 23 shows the result for one octant of the sphere under the axis-aligned loads at two corner points. The displacement along one axis is color-coded in Fig. 23b. Fig. 23c compares the convergence of the new bi-4 scheme to two other generalized IGA elements, built from [KP14] and from [NKP14].

(a) input mesh

(b) displacement

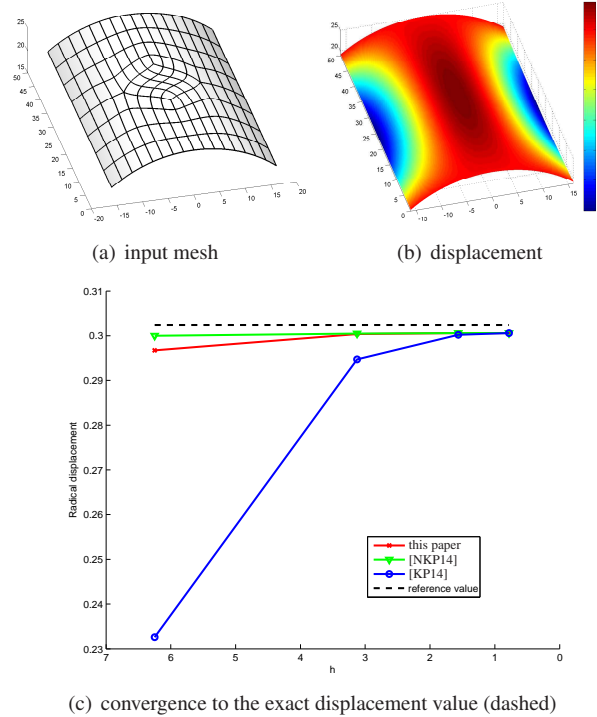(c) convergence to the exact displacement value (dashed)

Figure 24: Scordelis-Lo roof thin shell.

For the Scordelis-Lo roof, we intentionally chose an irregular quad mesh for approximation as shown in Fig. 24a. The error is measured by tracking the maximum displacement of the midpoint on the edge aligned with the cylinder's axis. We see that, despite the irregular layout, the value of this fourth-order differential equation converges to the benchmark value.

In Fig. 24c, the results of the analysis are compared to [KP14] and [NKP14], showing rapid convergence in all cases.

7. Discussion and Conclusion

We presented a surface cap construction of degree bi-4 that improves on the state of the art for layouts that include irregular points. The improvement has been validated as a good distribution of highlight lines on a collection of challenging test data and by using the caps for IGA computations. Remarkably both the exact G^1 bi-4 construction (for $n < 8$), and the 2×2 macropatch bi-4 construction for higher valences yield highlight lines on par with more sophisticated exact G^2 constructions. The constructions display better highlight lines than the existing algorithms of equal or lower degree. A complex guiding surface construction is baked into the formulas of the new bi-4 construction, thereby transferring the guide's good shape and approximation properties to the central point of the cap. The final formulas express the surface in terms of the B-spline-like quadrilateral control net with one generating function associated with each vertex of the control net.

The purely polynomial setup, of degree bi-4 means that evaluation and differentiation are cheap and generalized IGA is relatively easy to implement. It is convenient that the (isogeometric analysis) elements have as their degrees of freedom the vertices of the irregular quad mesh. As expected, the L^2 convergence rates are higher than those of linear elements, but stay around 9-10 for Poisson's equation on the disk, i.e. do not reach the 2^4 of Poisson's equation on the square without irregular points.

Acknowledgments.

[BC94] Klaus-Peter Beier and Yifan Chen. Highlight-line algorithm for realtime surface-quality assessment. *Computer-Aided Design*, 26(4):268–277, 1994.

[BH14] Georges-Pierre Bonneau and Stefanie Hahmann. Flexible G^1 interpolation of quad meshes. *Graphical Models*, 76(6):669–681, 2014.

[BM] Michel Bercovier and Tanya Matskewich. Smooth Bézier surfaces over arbitrary quadrilateral meshes. http://arxiv.org/abs/1412.1125.

[BSL+85] Ted Belytschko, Henryk Stolarski, Wing Kam Liu, Nicholas Carpenter, and Jame SJ Ong. Stress projection for membrane and shear locking in shell finite elements. *Computer Methods in Applied Mechanics and Engineering*, 51(1):221–258, 1985.

[CC78] E. Catmull and J. Clark. Recursively generated B-spline surfaces on arbitrary topological meshes. *Computer-Aided Design*, 10:350–355, September 1978.

[Far02] G. Farin. *Curves and Surfaces for Computer Aided Geometric Design: A Practical Guide*. Academic Press, San Diego, 2002.

[GP15] David Groisser and Jörg Peters. Matched G^k-constructions always yield C^k-continuous isogeometric elements. *Computer Aided Geometric Design*, 34:67–72, 2015.

[Gre74] J. A. Gregory. *Smooth interpolation without twist constraints*, pages 71–88. Academic Press, 1974.

[Gre94] G. Greiner. Variational design and fairing of spline surfaces. *Computer Graphics Forum*, 13(3):143–154, 1994.

[Gre96] G. Greiner. Curvature approximation with application to surface modeling. In J. Hoschek and P. Kaklis, editors, *Advanced Course on FAIRSHAPE*. B. G. Teubner, 1996.

[GZ94] John A. Gregory and Jianwei Zhou. Filling polygonal holes with bicubic patches. *Computer Aided Geometric Design*, 11(4):391–410, 1994.

[HCB05] T. J. R. Hughes, J. A. Cottrell, and Y. Bazilevs. Isogeometric analysis: CAD, finite elements, NURBS, exact geometry and mesh refinement. *Computer Methods in Applied Mechanics and Engineering*, 194:4135–4195, 2005.

[HKD93] Mark Halstead, Michael Kass, and Tony DeRose. Efficient, fair interpolation using Catmull-Clark surfaces. In *Proc 20th Annual Conference on Computer Graphics and Interactive Techniques*, SIGGRAPH '93, pages 35–44, New York, NY, USA, 1993. ACM.

[IZ68] B. M. Irons and O. C. Zienkiewic. The isoparametric finite element system a new concept in finite element analysis. In *Proc. Conf. Recent Advances in Stress Analysis. Royal Aeronautical Society. London.*, 1968.

[Koi70] WT Koiter. On foundations of linear theory of thin elastic shells. 1. *Proc Koninklijke Nederlandse Akademie van WetenSchappen, ser. B Phys. Sci.*, 73(3):169, 1970.

[KP14] Kęstutis Karčiauskas and Jörg Peters. Smooth multi-sided blending of biquadratic splines. *Computers and Graphics*, SMI 2014 Hongkong, 2014.

[KP15a] Kęstutis Karčiauskas and Jörg Peters. Biquintic G^2 surfaces via functionals. *Computer Aided Geometric Design*, pages 17–29, 2015.

[KP15b] Kęstutis Karčiauskas and Jörg Peters. Improved shape for multisurface blends. *Graphical Models*, xx:xx–xx, xx 2015. Dagstuhl workshop on Geometric Design, May 2014.

[KP15c] Kęstutis Karčiauskas and Jörg Peters. Quad-net obstacle course, 2015. http://www.cise.ufl.edu/research/SurfLab/shape_gallery.shtml.

[Lev06] Adi Levin. Modified subdivision surfaces with continuous curvature. *ACM Trans. Graph*, 25(3):1035–1040, 2006.

[LGS99] J. Loos, G. Greiner, and H-P. Seidel. Modeling of surfaces with fair reflection line pattern. In Bob Werner, editor, *Proceedings of the International Conference on Shape Modeling and Applications (SMI-99)*, pages 256–263, Los Alamitos, CA, March 1–4 1999. IEEE Computer Society.

[LS08] Charles T. Loop and Scott Schaefer. G^2 tensor product splines over extraordinary vertices. *Comput. Graph. Forum*, 27(5):1373–1382, 2008.

[LSNC09] Charles T. Loop, Scott Schaefer, Tianyun Ni, and Ignacio Castaño. Approximating subdivision surfaces with Gregory patches for hardware tessellation. *ACM Trans. Graph*, 28(5):151:1–151:9, 2009.

[NKP14] Thien Nguyen, Kęstutis Karčiauskas, and Jörg Peters. A comparative study of several classical, discrete differential and isogeometric methods for solving poisson's equation on the disk. *Axioms*, 3(2):280–299, 2014.

[PBP02] Hartmut Prautzsch, Wolfgang Boehm, and Marco Paluszny. *Bézier and B-spline techniques*. Springer Verlag, 2002.

[Pra97] H. Prautzsch. Freeform splines. *Comput. Aided Geom. Design*, 14(3):201–206, 1997.

[Rei93] U. Reif. *Neue Aspekte in der Theorie der Freiformflächen beliebiger Topologie*. PhD thesis, Universität Stuttgart, 1993.

[Rei98] U. Reif. TURBS—topologically unrestricted rational B-splines. *Constr. Approx.*, 14(1):57–77, 1998.

[Sar00] Ramon F. Sarraga. A variational method to model G^1 surfaces over triangular meshes of arbitrary topology in R^3. *ACM Trans. Graph*, 19(4):279–301, 2000.

[SSE+13] M. A. Scott, R. N. Simpson, J. A. Evans, S. Lipton, S. A. Bordas, T. J. R. Hughes, and T. W. Sederberg. Isogeometric boundary element analysis using unstructured T-splines. *Comput. Methods Appl. Mech. Eng.*, 254:197–221, 2013.

[Tut15] Autodesk Tutorial. http://help.autodesk.com/view/alias/2015/enu/?guid=guid-2fce06eb-8ef7-4507-92f7-82a73a0df378, 2015. accessed Jan 16.

[WN01] Geir Westgaard and Horst Nowacki. Construction of fair surfaces over irregular meshes. In *Symposium on Solid Modeling and Applications*, pages 88–98, 2001.
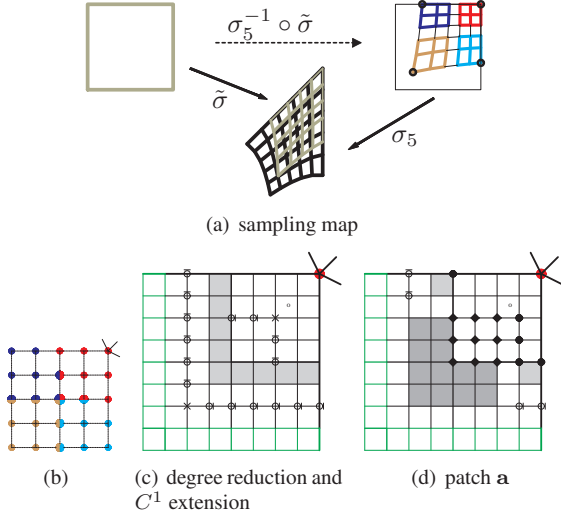
Appendix A: Guides for macro-patches

(a) sampling map

(b)   (c) degree reduction and   (d) patch **a**
         C^1 extension

Figure 25: 2×2 **construction**: transferring the shape of the guide surface to the bi-4 patches. (b) The pattern of sampling and overlap averaging. (c) BB-coefficients set by degree reduction are indicated by $\circ|$, $\bar{\circ}$ and $\times$. The grey underlaid coefficients are set by C^1 extension.

The symmetric planar map σ_4 consists now of 2×2 pieces and we may focus on one sector. We name σ_4^o the piece touching the central point $\mathbf{0}$ (see Fig. 25). We choose the border from χ, the characteristic map of Catmull-Clark subdivision, extend the data by reparameterization and splitting to define the BB-net rendered in green in Fig. 25c,d, and resolve the G^1 constraints symbolically. To make the control net as uniform as possible, we set additionally $\dot{\mathbf{p}}_{20} := 2\dot{\mathbf{p}}_{10}$ (where $\dot{\mathbf{p}}_{00} := \mathbf{0}$). This leaves five free parameters. The BB-coefficients of $\mathbf{J}_{\mathbf{s},1}^4 \sigma_4^o$, where $\mathbf{s}$ is the point common to the four subpatches provides another four free parameters. Applying the degree reduction (16), determines the BB-coefficients marked $\circ|$, $\bar{\circ}$ and $\times$ (as the average of rules $\circ|$ and $\bar{\circ}$) in Fig. 25c. The BB-net underlaid in grey is obtained by C^1 extension of σ_4^o. This leaves γ in (14) as the final tenth free parameter. Having eliminated dependent BB-coefficients symbolically so far, we set the ten parameters by minimizing numerically the functional $\mathcal{F}_{2,3}$ over all four subpatches of σ_4. In particular, this yields the formula for γ_{def} in (14).

We calculate numerically $\sigma_5^{-1} \circ \tilde{\sigma}$, where $\tilde{\sigma} := \lambda^{-1}\sigma_4^o$ (see Fig. 25a), and λ is the subdominant eigenvalue of Catmull-Clark subdivision. (Experiments show that if we set $\tilde{\sigma} := \sigma^o$ without the virtual Catmull-Clark step when applying the bi-5 guide, the shape is worse.) An intermediate bi-4 2×2 macro-patch **a** is constructed as follows. We apply one Catmull-Clark subdivision step to the initial CC-net and sample the bi-5 guide surface **g** using $\sigma_5^{-1} \circ \tilde{\sigma}$. The samples $\mathbf{J}_{\mathbf{s},2}^4(\mathbf{g} \circ \sigma_5^{-1} \circ \tilde{\sigma})$ are averaged at some overlapping locations as indicated in Fig. 25b to yield the central bi-4 patch $\mathbf{a}^o$. Applying the strategy illustrated in Fig. 25c (including first the correction of the sampled patch $\mathbf{a}^\circ$ via the degree-reduction operations $\circ|$, $\bar{\circ}$ and $\times$) yields the full macro-patch **a**.

As in Section 3, the quadratic expansion at the central point $\mathbf{0}$, reparameterized by $\sigma_4^{k,o}$, is expressed in terms of the BB-coefficients (red disks in Fig. 5) closest to the irregular point. This leaves as degrees of freedom in the G^1 strips the BB-net indicated by black disks in Fig. 25d. The remaining BB-coefficients are pinned down by the G^1 constraints and the degree reduction (16). The BB-net marked by black diamonds are free to choose, while the grey underlay indicates that we choose a C^2 extension to the adjacent subpatches. Overall this leaves $13n$ free points. These are fixed by minimizing the functional $\mathcal{F}_4$ over the differences between $4n$ subpatches of $\mathbf{p}^k$ and $\mathbf{a}^k$.

Note that, of the four pieces of the macro-patch, only the one closest to the irregular point needs to be tabulated since the other ones are defined by simple formulas of C^2-extension at the junction of the four pieces, C^1-extension between pieces of the G^1 strips, the G^1-extension of the tensor-border data and pattern (16).